Electronic Supplementary Information for:

High rate lithium-ion batteries from hybrid hollow spheres with few-layered MoS_2-entrapped carbon sheath synthesized with a space-confined reaction

Zhuang Sun, [a] Yuchen Yao, [a] Jing Wang, [b] Xuefeng Song,*[a] Peng Zhang, [a] Liping Zhao, [a] and Lian Gao*[a]

[a.] *State Key Laboratory for Metallic Matrix Composite Materials, School of Materials Science and Engineering, Shanghai Jiao Tong University, Shanghai, 200240, China.*

[b.] College of Energy, Nanjing Tech University, 30 Puzhu Road, Nanjing 211816, P. R. China.

*E-mail address: liangao@mail.sic.ac.cn (L. Gao); songxfeng@sjtu.edu.cn (X. F. Song)

Tel: +86-12-52412718. Fax: +86-21-52413122

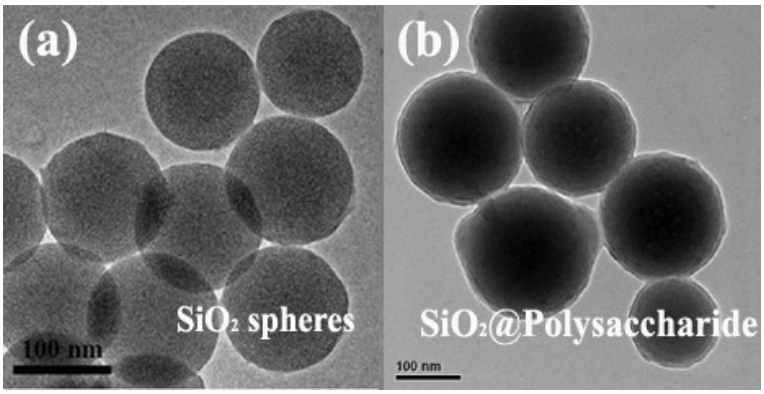

Figure S1. TEM images of (a) amino-functionalized silica spheres and (b) silica@polysaccharide core-shell spheres.

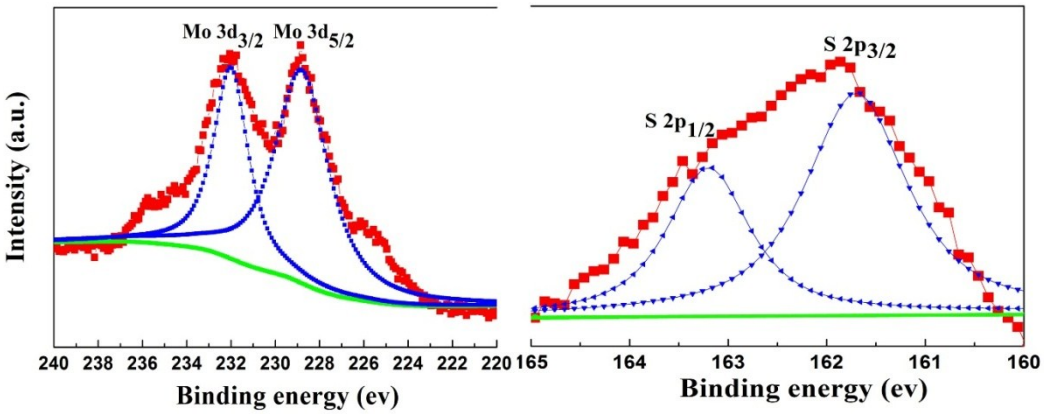

Figure S2. Chemical composition analysis by X-Ray photoemission spectroscopy (XPS) for Mo and S spectrum taken from the as-obtained product before annealing. The observation of Mo $3d_{3/2}$ and Mo $3d_{5/2}$ peaks at 229.2 and 233.8 eV suggests the presence of Mo^{5+} ions.[1] The S 2p spectrum can be interpreted in terms of two doublets, with S $2p_{1/2}$ and S $2p_{3/2}$ binding energies of 161.8 and 163.4 eV, which is similar to those of amorphous MoS_3.[2] Furthermore, the S/Mo elemental ratio estimated from the integrated peak area of XPS spectra is 2.8, which also suggests the as grown molybdenum sulfide before annealing is stoichiometrically close to MoS_3. Therefore, the exact phase of the molybdenum sulfide in the as-obtained product may be the mixture of MoS_2 and MoS_3.

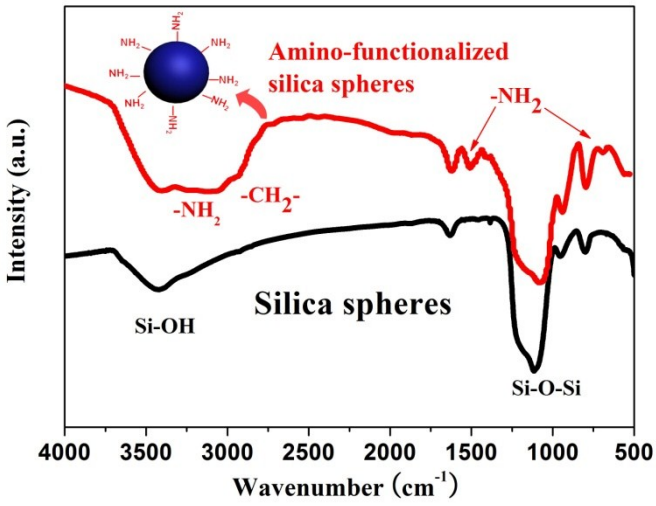

Figure S3. Fourier transform infrared (FT-IR) spectra. FT-IR spectroscopy was performed to characterize the bare silica spheres and amino-functionalized silica spheres. The spectrum of functionalized silica spheres showed three peaks of amino groups on the surface of the templates, which were different from that of bare silica spheres. The abundant amino groups can serve as nucleation sites and deposition places to couple Mo precursor and coat glucose-derived carbon precursor, resulting in corresponding MoS_x ($2<x<3$) and polysaccharide anchored on the surface of silica under suitable solvothermal reaction condition.

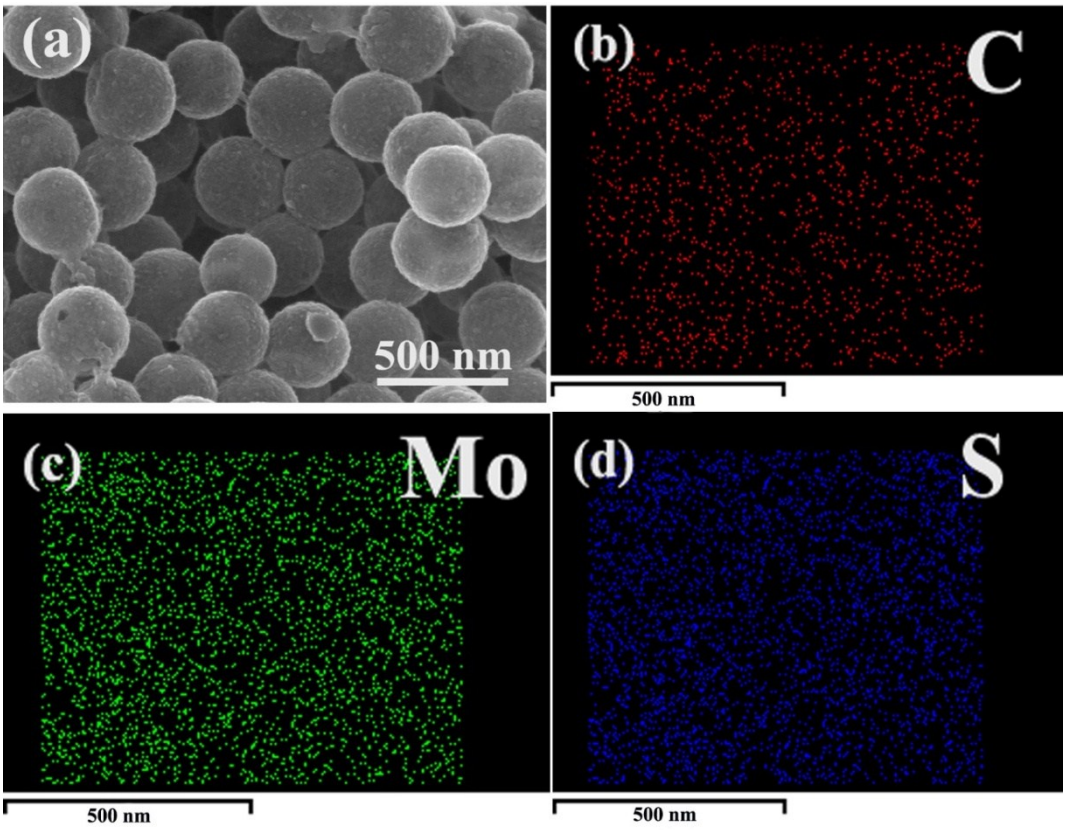

Figure S4. SEM image of HFMEC (a) and its EDX element mapping profile of carbon (b), molybdenum (c), and sulfur (d) elements.

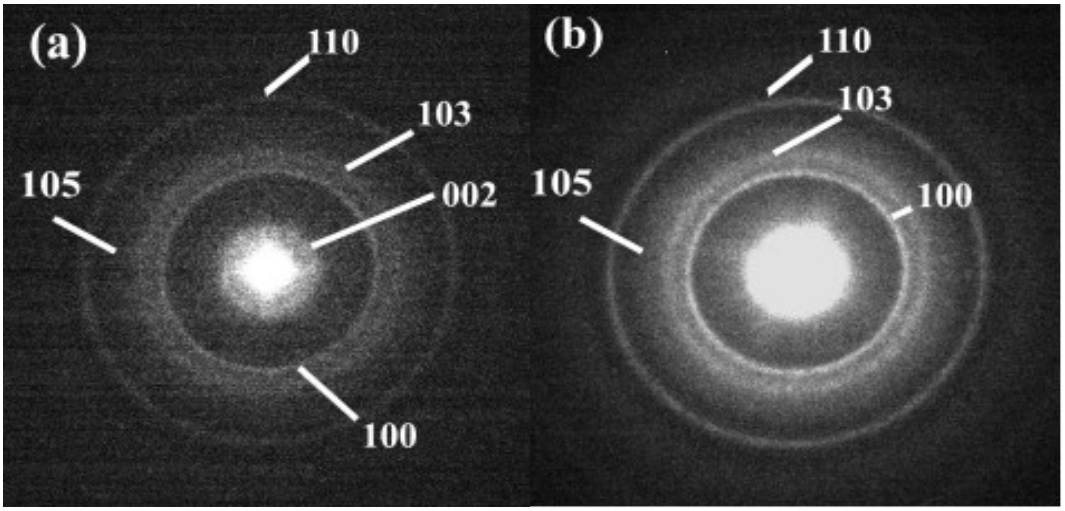

Figure S5. SAED patterns of (a) HFMEC and (b) HMOC.

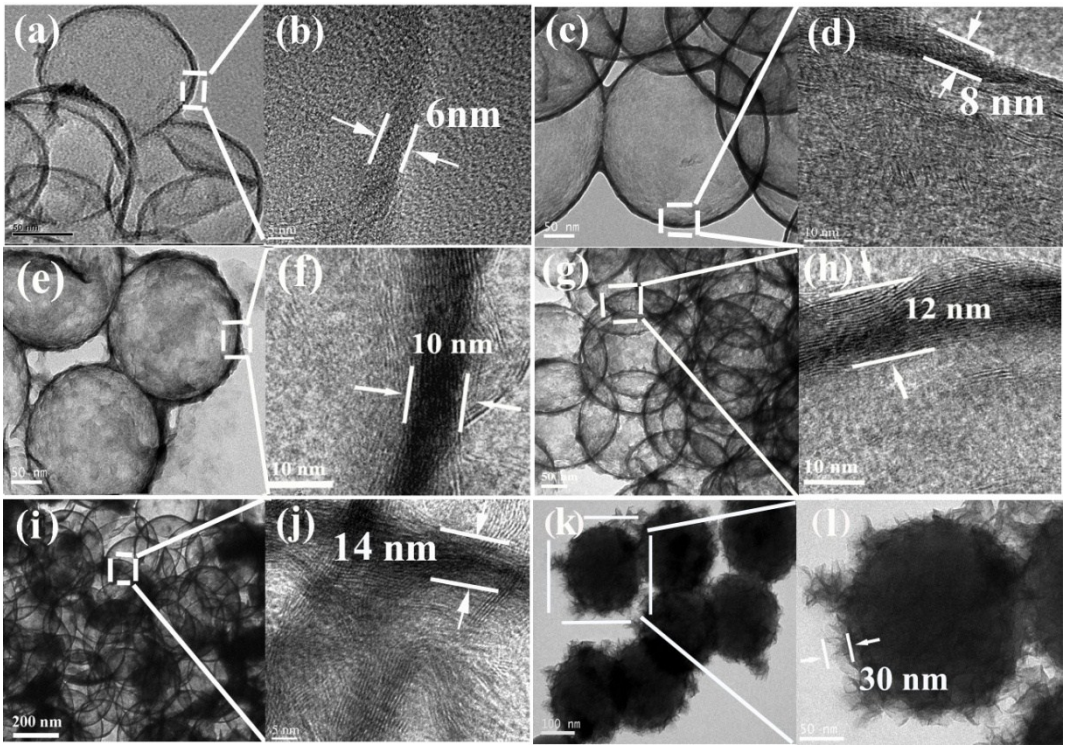

Figure S6. TEM and HRTEM images of as-obtained product at different ratio of ammonium thiomolybdate to glucose: (a, b) without addition of ammonium thiomolybdate, (c, d) 1:4, (e, f) 1:3.5, (g, h) 1:3, (i, j) 1:2 and (k, l) without additon of glucose.

In order to investigate the effect of the ratio of ammonium thiomolybadate/glucose on the shell thickness and morphology of the HFMEC, a serious of parallel experiments were performed. First, when the mixture of glucose and silica template without adding ammonium thiomolybdate was treated under the same condition as that for the preparation of HFMEC, it can be found that the as-obtained product is just hollow carbon spheres without any lattice fringes in the shell and the shell thickness is ~6 nm (Fig. S6a,b). When the mass ratio of the ammonium thiomolybdate/glucose is 1:4, the lattice fringes of MoS_2 sheets can be found (Fig. S6c,d). In addition, from Fig. S6d, it is obvious that the layeres of MoS_2 are extremely thin and small, and the thickness of the hybrid shell is ~8 nm. As the mass ratio increases to 1:3.5, the lattice fringes of MoS_2 sheets in the shell are

more obvious (Fig. S6e,f), and the thickness increased to ~10 nm. When the mass ratio increases to 1:3, HFMEC with ~91 wt% MoS_2 nanosheets in the hybrid can be obtained as shown in the Fig. S6g,h), in which MoS_2 is dominant in the hybrid shell, and intervolve carbon components randomly. The thickness of the hybrid shell increased to ~12 nm. When the mass ratio of ammonium thiomolybdate/glucose continues to increase to 1:2, the shell thickness is ~14 nm, which is quite similar with the hybrid (1:3). However, bare MoS_2 sheets could be found outside the HFMEC (Fig. S6i,j), indicating the optimum mass ratio of the ammonium thiomolybdate/glucose is 1:3. Furthermore, wihout addition of glucose, it is obvious that MoS_2 nanosheets anchored randomly on the surface of amino-functionalized silica spheres (Fig. S6k, l), and the shell thickness of MoS_2 layers outside is ~30 nm, which is quite larger than that of HFMEC. This factor indicates that during the process of synthesis of HFMEC, the carbon matter greatly inhibit the restacking of MoS_2 layers. In addition, the mass contents of MoS_2 in the as-obtained products with different ratio of ammonium thiomolybdate to glucose determined by TGA-method is 61 wt% (1:4), 83 wt% (1:3.5), 91 wt% (1:3) and 96 wt% (1:2) , respectively (Fig. S7). Therefore, it is found that the thickness of the hybrid shells and the content of MoS_2 in the HFMEC can be tuned by adusting the ratio of MoS_2 precursor to carbon precursor under the same conditions. With an optimum ratio of MoS_2 precursor to carbon precuror, ultrathin hybrid shells with large content of MoS_2 (HFMEC-91) can be obtained.

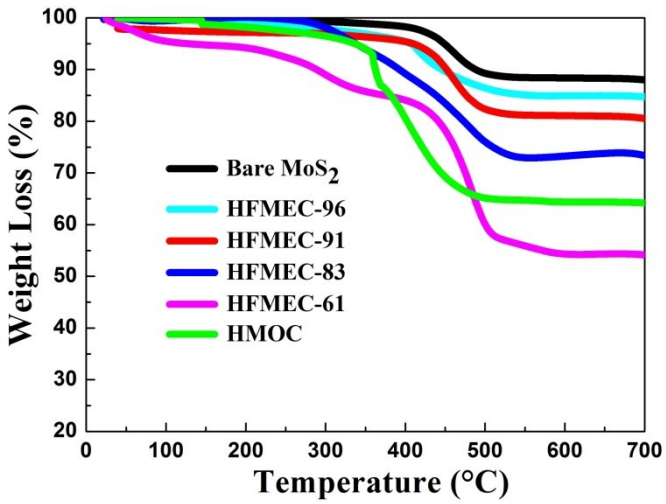

Figure S7. TGA curves of bare MoS_2, HMOC and HFMEC with different MoS_2 content (HFMEC-61: HFMEC with 61 wt% MoS_2; HFMEC-83: HFMEC with 83 wt% MoS_2; HFMEC-91: HFMEC with 91 wt% MoS_2; HFMEC-96: HFMEC with 96 wt% MoS_2) measured under air atmosphere. Let the weight percentage of MoS_2 in the HFMEC to be x. Assuming the carbon content is completely removed after combustion, for instance, 0.88 x = 0.80. Therefore x = 0.91. From this calculation, the carbon content is ~9 wt% for HFMEC-91.

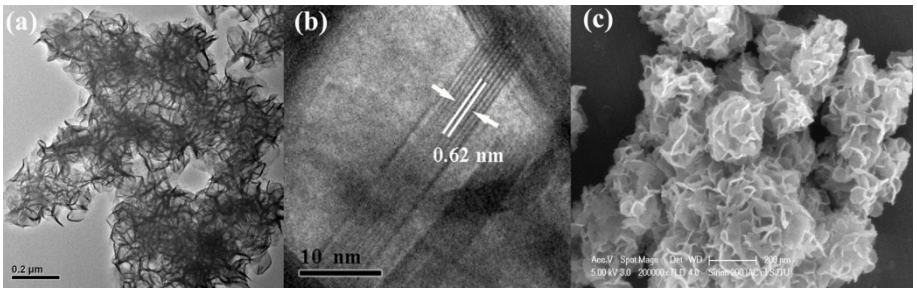

Figure S8. (a) TEM, (b) HRTEM and (c) SEM images of the bare MoS_2 nanosheets. In absence of glucose and silica templates, the MoS_2 particles aggregate to form large MoS_2 lumps as verified by the TEM and SEM images.

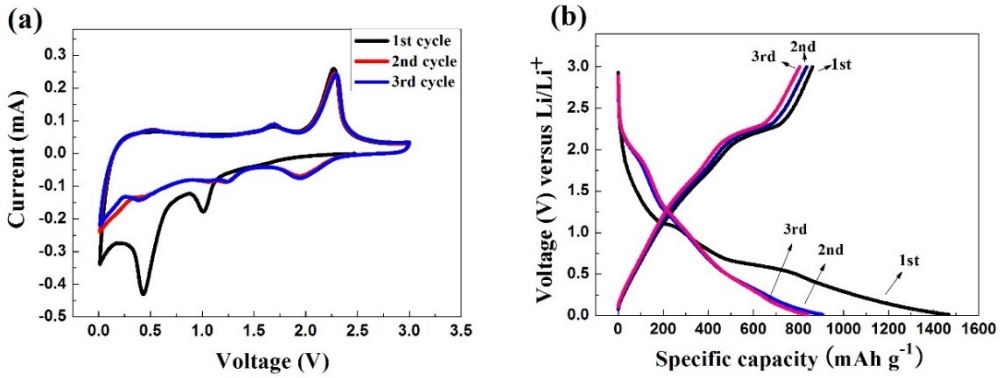

Figure S9. (a) Cyclic voltammetry curves of the HMOC elecotrode showing the initial three cycles between 3 V and 0.01 V at a scan rate of 0.1 mV s^{-1}. (b) Galvanostatic charge/discharge curves of HMOC electrode at a current density of 50 mA g^{-1}.

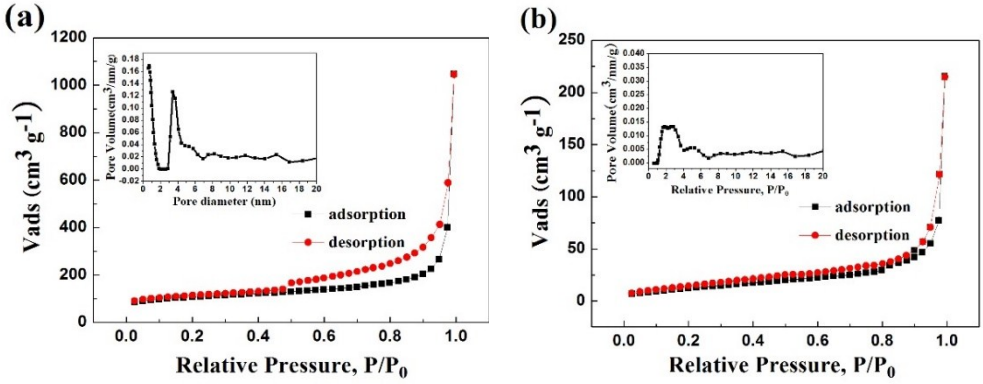

Figure S10. Nitrogen adsorption-desorption with corresponding pore size distributions (inset) of HMOC and HFMEC samples. Compared with HFMEC, HMOC possess much larger surface area, which may result from the ultrathin MoS_2 nanosheets on the outer surface and the hollow carbon spheres. Furthermore, the higher carbon content in the HMOC leads to more micro-, meso- pores in the amorphous carbon (the pore volumes of HMOC and HFMEC are 0.71 and 0.14 cm^3 g^{-1}, respectively), which enhance the inner surface area.

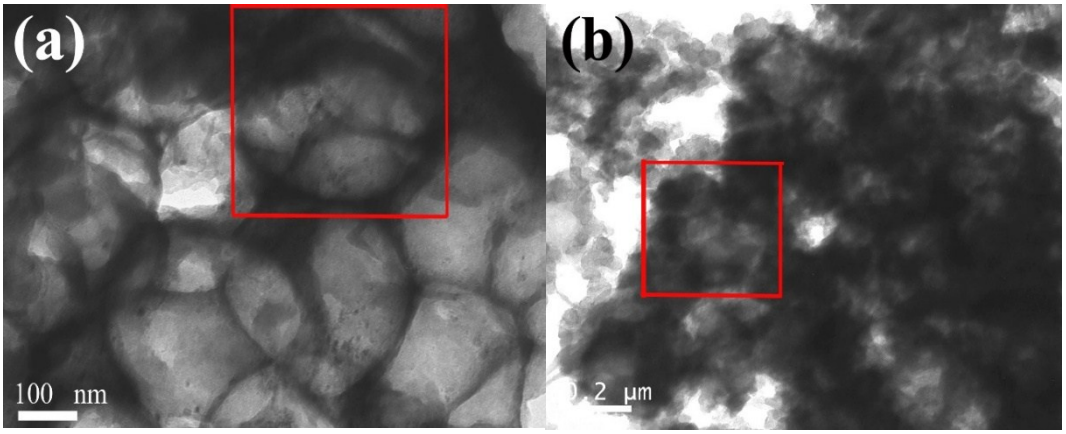

Figure S11. TEM images of the (a) HFMEC and (b) HMOC samples after 100 cycles.

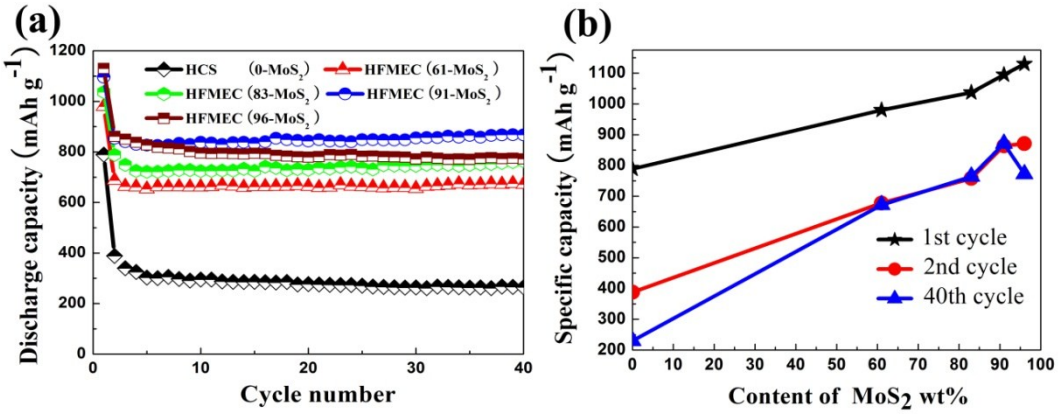

Figure S12. (a) Cycling stability of hollow carbon spheres and HFMEC with various MoS_2 content tested in the range of 0.01-3.0 V vs Li^+/Li at the current density of 200 mA g^{-1}; (b) Variation of discharge capacity as a function of MoS_2 weight fraction.

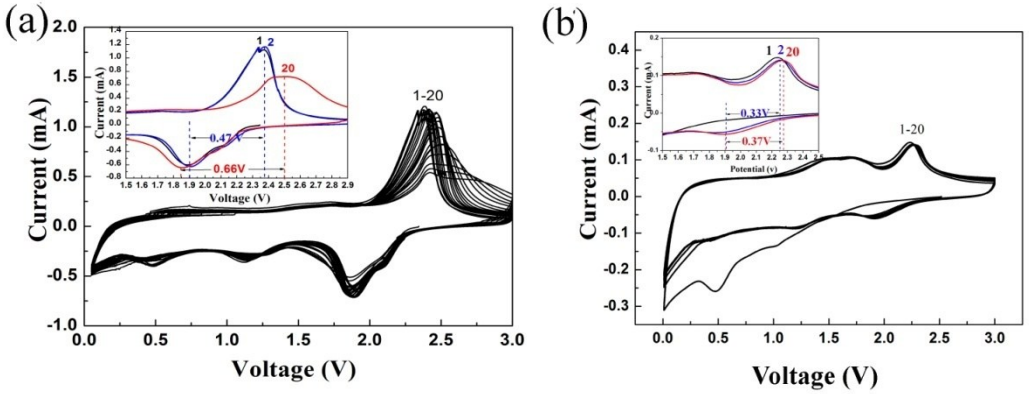

Figure S13. Cyclic voltammetry curves of the (a) MoS_2 and (b) HFMEC electrode between 3 V and 0.01 V at a scan rate of 0.5 mV s^{-1}.

The difference between charge and discharge plateau potentials can represent the degree of polarization of the electrode.[16-18] As can be seen from the cyclic voltammetry curves from 1st to 20th cycle (Fig. S13), the values of the differences between the anode and cathode peaks for the HFMEC (2nd: 0.33 V, 20th: 0.37 V) are much smaller than those of bare MoS_2 electrode (2nd: 0.47 V, 20th: 0.66V) from 1st cycle to 20th cycle at 0.5 mV S^{-1}, which indicates that the HFMEC electrode has lower polarization and better reaction kinetics, because of the improved electrical conductivity provided by the carbon matter and much smaller charge transfer resistance in the hybrid compared to the bare MoS_2.

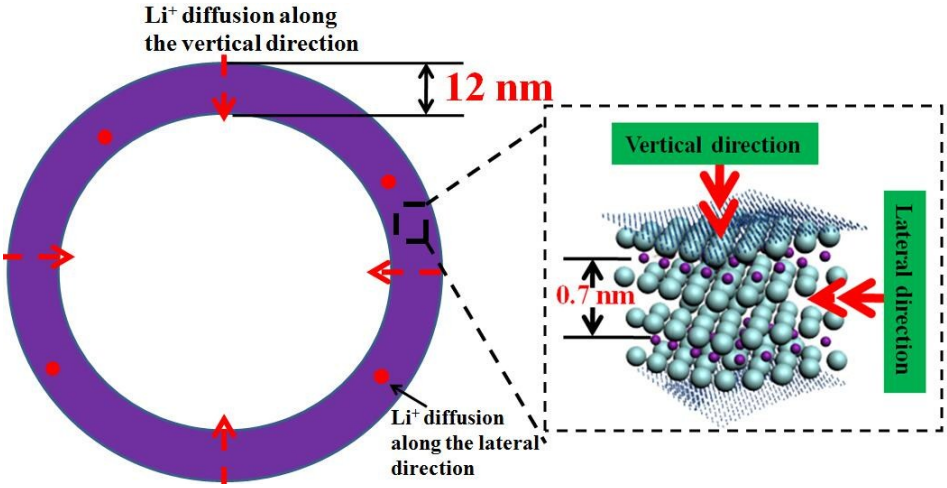

Scheme S1. Scheme images of Li ions rapid diffusion in HFMEC along the two directions; The vertical and lateral direction is perpendicular and parallel to the basal plane of MoS_2, respectively.

Table S1. The content of carbon in various MoS_2-carbon composites.

Materials	The content of carbon in the composites (wt%)	Ref.
HFMEC	9~39	This work
HMOC	27	This work
Graphene-like MoS_2/amorphous carbon nanocomposite	35.3	Ref.3
Few-layer MoS_2 anchored on carbon nanosheet	22.9	Ref.4
Porous and free-standing MoS_2/GS hybrid	19~51	Ref.5
MoS_2@CMK-3 nanocomposite	19.4	Ref.6
Hierarchical quasi-hollow MoS_2 microsphere encapsulated porous carbon	26.4	Ref.7
Hollow MoS_2-carbon nanocomposites	28	Ref.8
MoS_2 nanosheets on carbon nanotubes	20	Ref.9
Single-layered MoS_2 embedded incarbon nanofibers	38	Ref.10
MoS_2-C nanowires/ nanotubes	22 / 36	Ref.11
Ultrathin MoS_2 nanosheets supportedon N-doped carbon nanoboxes	19	Ref.12
Carbon coated MoS_2 flower-like nanostructure	23	Ref.13
Hierarchical MoS_2 shells supported on carbon spheres	25	Ref.14
MoS_2/carbon anode with three-dimensional flower-like architecture	33	Ref.15

Reference

1. Y. H, Chang. C. T. Lin, T. Y. Chen, C. L. Hsu, Y. H. Lee, W. J. Zhang, K. H. Wei and L. J. Li, *Adv. Mater.,* 2013, **25,** 756.
2. Y. M. Shi, Y. Wang, J. I. Wong, S. Y. S. Tan, C. L. Hsu, L. J. Li, Y. C. Lu and H. Y. Yang, *Sci. Rep.,* 2013, **3,** 2169.
3. K. Chang and W. X. Chen, *J. Mater. Chem.,* 2011*,* **21***,* 17175.
4. J. W. Zhou, J. Qin, X. Zhang, C. S. Shi, E. Z. Liu, J. J. Li, N. Q. Zhao and C. N. He, *ACS Nano,* 2015, **9**, 3837.
5. R. H. Wang, C. H. Xu, J. Sun, Y. Q. Liu, L. Gao, H. L. Yao and C. C. Lin, *Nano Energy*, 2014, **8,** 183.
6. X. S. Zhou, L. J. Wan and Y. G. Guo, *Nanoscale,* 2012, **4**, 5868.
7. Z. M. Wan, J. Shao, J. J. Yun, H. Y. Zheng, T. Gao, M. Shen, Q. T. Qu and H. H. Zheng, *Small,* 2014, **10**, 4975.
8. J. Jin, B. Kim, M. Kim, N. Park, S. Kang, S. M. Lee, H. J. Kim and S. U. Son, *Nanoscale,* 2015, **7**, 11280.
9. S. K. Park, S. H. Yu, S. Woo, B. Quan, D. C. Lee, M. K. Kim, Y. E. Sung and Y. Piao, *Dalton Trans*., 2013, **42**, 2399.
10. C. B. Zhu, X. K. Mu, P. A. van Aken, Y. Yu and J. Maier., *Angew. Chem.,* 2014, **126**, 2184.
11. C. F. Zhang, Z. Y. Wang, Z. P. Guo and X. W. Lou, *ACS Appl. Mater. Interfaces,* 2012, **4**, 3765.
12. X. Y. Yu, H. Hu, Y. W. Wang, H. Y. Chen and X. W. Lou, *Angew. Chem. Int. Ed.,* 2015, **54**, 7395.
13. S. Hu, W. Chen, J. Zhou, F. Yin, E. Uchaker, Q. F. Zhang and G. Z. Cao, *J. Mater. Chem. A,* 2014, **2**, 7862.
14. L. Zhang and X. W. Lou, *Chem. Eur. J.,* 2014, **20**, 5219.
15. J. J. Wang, C. Luo, T. Gao, A. Langrock, A. C. Mignerey and C. S. Wang, *Small,* 2015, **11**, 473.
16. P. G. Bruce, B. Scrosati and J. Marie, *Angew. Chem. Int. Ed.,* 2008, **47**, 2930.
17. Y. Shi, L. Wen, F. Li and H. M. Cheng, *J. Power Sources,* 2011, **196**, 8610.
18. Z. Hu, L. X. Wang, K. Zhang, J. B. Wang, F. Y. Cheng, Z. L. Tao and J. Chen, *Angew. Chem.,* 2014, **126**, 13008.